

Contact-driven delamination and spalling of coatings due to cyclic shock heating

A.S. Semenov^{a,*}, H.-A. Bahr^a, H. Balke^a, H.-J. Weiss^b

^aDepartment of Mechanical Engineering, Dresden University of Technology, Mommsenstrasse 13, 01062 Dresden, Germany

^bFraunhofer Institute for Material and Beam Technology, Winterbergstrasse 28, 01277 Dresden, Germany

Received 20 June 2003; received in revised form 8 October 2003; accepted 8 July 2004

Available online 22 October 2004

Abstract

A new debonding mechanism taking into account crack face contact caused by a thermal gradient during laser heating is considered. The contact renders double influence on the energy release rate G : it leads to sharp increase of G at convergence of two cracks and decreases steady-state value of G . The first feature can explain the laser-induced spalling of thermal barrier coating under combined action of sintering and heating. The inhomogeneous temperature through coating thickness under laser heating can induce contact-driven debonding leading to the spalling under convergence of two cracks. The loading conditions of contact occurrence are derived. The simplified models of contact-driven debonding are proposed and compared with finite element solution.

© 2004 Elsevier B.V. All rights reserved.

PACS: 46.30.Nz; 62.20.Mk; 68.60.Bs; 46.30.P; 42.62.-b

Keywords: Coatings; Computer simulation; Delamination and spalling; Contact

1. Introduction

Laser beam heating serves as a suitable and efficient test for the resistance of coatings to debonding and spalling under thermal shock [1–5]. Spalling due to localized hot shock has been investigated in Ref. [6] as an edge effect. In the presence of a delamination crack, the compressive stress due to transient heating may give rise to buckling and subsequent further delamination or spalling, as considered in Refs. [1,7]. However, as cracks in coatings usually arise as a result of sintering and/or high-temperature creep, the effect of these processes, too, has to be taken into account.

It may give rise to a different course of events also proceeding through several stages of damage with increasing number of thermal cycles (Fig. 1): vertical cracking → delamination → spalling, as observed in sprayed [8] and electron beam-deposited [3,4] thermal barrier coatings (TBCs) and wear-resistant layers on hard metals [9]. Vertical crack formation and delamination can be understood as a

result of the combined action of high-temperature creep under compressive thermal stress and sintering of the porous ceramic [3,4,10]. Both mechanisms lead to high tensile stress building up while cooling down to room temperature after cyclic heating. It is not quite obvious then how the spalling is brought about in the case of vertical cracks which do not close under heating: The energy release rate of the converging delamination cracks decreases so that delamination stops (crack arrest phenomenon) [11,12] (see insert in Fig. 2a). As a clue to the possible mechanism, delamination and spalling are observed during the heating phase of the cycle only (see results of temperature measurement during cycle in Fig. 3). This was also observed in Ref. [2] on graded coatings for gas turbines.

Inhomogeneous temperature due to transient heating causes bending of the detached part of the subsurface layer and sequential contact with the substrate that may give rise to final detachment. A new model of spalling fracture based on this idea is developed in present paper. The contact force at the edge of the debonded layer provides an increasing energy release rate with decreasing attachment length ΔL (Fig. 2b).

* Corresponding author. Tel.: +49 351 46335263; fax: +49 351 46332450.

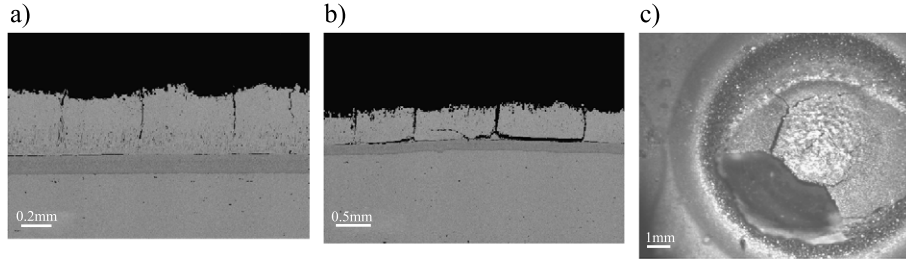


Fig. 1. Progress of damage in EB-PVD TBC during laser cycling at $T_{\max}=1500\text{ }^{\circ}\text{C}$ [3,4]: (a) vertical cracks initiation (number of cycles $N=30$); (b) delamination crack propagation ($N=1400$); (c) spalling ($N=1439$).

The present approach can be regarded as an extension of the debonding analysis in Ref. [11] and delamination analysis of TBCs subjected to a thermal gradient in Ref. [13] by taking into account the eventually present contact due to bending moment (Fig. 4). The article is organized as follows. In Section 2, the analysis of contact-driven steady state debonding is presented. In Section 3, a simple analytical model for the increasing energy release rate of two approaching cracks is considered. Finally, in Section 4, the results of FE analysis of (unsteady-state) debonding of TBC under transient laser heating taking into account contact of crack faces are discussed.

2. Contact-driven steady-state debonding

2.1. Surface layer spalling

The effect of crack face contact on delamination crack propagation is considered in the following by simplified models first, providing steady-state solutions where propagation does not depend on crack length [7]. This is realized for crack length a well exceeding the height h as pictured in Fig. 4. The problem of subsurface crack in a semi-infinite homogeneous plate was solved by Thouless et al. [14] for the absence of crack face contact (Fig. 4a). The present analysis takes into account the contact for finite crack length as in Fig. 4b. Friction is neglected.

The structure is loaded as shown in Fig. 4a, P and M denoting force and moment, respectively, per unit length in third dimension. P and M follow from the stress distribution $\sigma(y)$ present in the layer in the absence of cracks (see Appendix A). Their sign is defined as in Fig. 4a.

Crack face contact is eventually realized at the edge and/or crack tip as indicated in Fig. 4b. The cases will be considered separately below. They differ essentially from the well-known extremely small contact area at the tip of interface cracks as described in Refs. [15,16]. The type of crack face contact considered here concerns homogeneous material, too.

A simple model for the analysis of the considered phenomena is proposed below. Its usefulness is evaluated by comparing the results with those of FE computations.

2.2. Edge contact

In the case of no contact at the edge (see Fig. 4a), the well-known relations for the stress intensity factors are given by [14]:

$$K_I = \frac{1}{\sqrt{2h}} \left[P \cos \omega + 2\sqrt{3} \frac{M}{h} \sin \omega \right], \text{ (contact absent)} \quad (1)$$

$$K_{II} = \frac{1}{\sqrt{2h}} \left[P \sin \omega - 2\sqrt{3} \frac{M}{h} \cos \omega \right], \text{ (contact absent)} \quad (2)$$

where the $\omega=52.07^{\circ}$ [7]. For plane strain, the energy release rate follows from Eqs. (1) and (2) as:

$$G_a = \frac{1 - \nu^2}{2Eh} \left(P^2 + 12 \frac{M^2}{h^2} \right), \text{ (contact absent)} \quad (3)$$

where E and ν denote Young's modulus and Poisson's ratio.

The contact at the edge is occurred in the case of considerable negative moment M . The value of P has no pronounced influence on the condition of edge contact (for a discussion of edge contact conditions, see Section

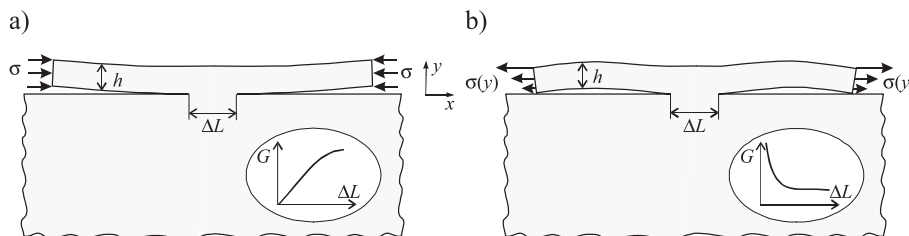


Fig. 2. Convergent debonding of surface layer due to edge loads. (a) Delamination due to sintering/creep (compare Ref. [11]). (b) Contact-driven debonding due to inhomogeneous heating. Inserts show the effect of edge contact on energy release rate $G(\Delta L)$.

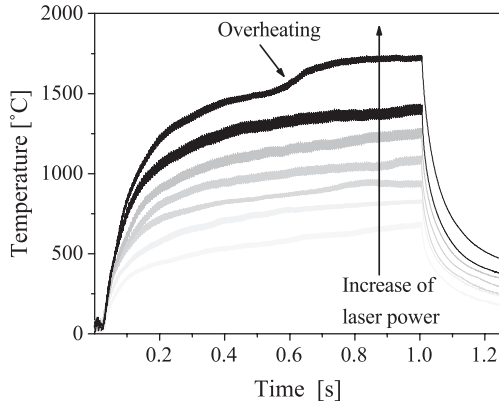


Fig. 3. Overheating (kink in the upper curve) is related to a sudden increase of thermal flow resistance due to delamination during 1-s-heating phase of an 11-s laser cycle [3,4].

2.5). With friction supposed to be absent, the contact acts with a normal force R (Fig. 5), which, together with P and M , has influence on stress intensity factors. The value of vertical reaction R is defined by the value of external applied moment M and can be evaluated on the base of simple model depicted in Fig. 5.

The analysis of the rigid-support model (presented in Fig. 5) performed on the base of Bernoulli–Euler beam theory gives the following value for the reaction R :

$$R(M) = \begin{cases} -\frac{3}{2} \frac{M}{a}, & M < 0 \\ 0, & M \end{cases} \quad (4)$$

The bending moment at the crack tip, of course, is affected by contact reaction force: $M_{tip} = M + Ra = -M/2$. Substituting M_{tip} for M in Eqs. (1)–(3) yields

$$K_I = \frac{1}{\sqrt{2h}} \left[P \cos \omega - \sqrt{3} \frac{M}{h} \sin \omega \right], \text{ (contact present)} \quad (5)$$

$$K_{II} = \frac{1}{\sqrt{2h}} \left[P \sin \omega + \sqrt{3} \frac{M}{h} \cos \omega \right], \text{ (contact present)} \quad (6)$$

$$G_p = \frac{1 - \nu^2}{2Eh} \left(P^2 + 3 \frac{M^2}{h^2} \right). \text{ (contact present)} \quad (7)$$

The comparison of Eqs. (3) and (7) shows that the edge contact reduces the energy release rate, in the case $P=0$ for example, by a factor 4. The effect vanishes for $M=0$.

2.3. Finite element analysis of delamination with edge contact

The accuracy of the results of Eqs. (5)–(7) as obtained from the simplified model was checked by finite element (FE) computations. The mesh used in calculating the problem of Fig. 4b is shown in Fig. 6 together with the resulting displacements, 10 times magnified. The FE computations have been performed with the aid of MSC.Marc code [17]. The 2D-mesh of 8-noded isoparametric finite elements with four integration points for stiffness matrix computation is used. The number of elements is about 4500. A highly refined self-similar focused mesh is used in the vicinity of the crack tip (see extended fragment of tip in Fig. 6). The size of elements around the crack tip is about $h/240$. The width and depth of substrate are taken equal to about $60h$, which gives a sufficiently good approximation to infinity for the case $a < 15h$. The substrate bottom is constrained against vertical displacement but free to displace horizontally. The right and left sides of the model are fixed in horizontal direction. The comparison of the obtained numerical results with the analytical solution for the half-plane (Eq. (3)) for the case no-contact [14] (see also Fig. 4a) shows the difference, which does not exceed 2% for wide ranges of M and P .

The direct constraint method [17] for the solution of the contact problem is used for the analysis of deformable-to-deformable contacts taking place between crack faces during heating. No special interference elements are required in this procedure and complex changing contact conditions can be simulated since no a priori knowledge of contact location is necessary. The friction between crack faces was neglected in computations.

The FE results in Fig. 7 show that the $G(a)$ curves, in either case, quickly approach the value given by the analytical solutions (3) and (7) (dashed lines) for the steady-state limit. The agreement is better than 1.5% for $a/h > 10$. Since the curves are normalized by the constant G_a as defined in Eq. (3), the upper curve in Fig. 7 approaches unity.

The good agreement between the analytical solutions for the steady-state limits (Eqs. (3) and (7)) and the FE results in the case of contact has been verified in wide ranges of P and M (Fig. 8), with a/h kept constant at the arbitrarily chosen value of about 10, which serves here as a suitable substitute for infinity.

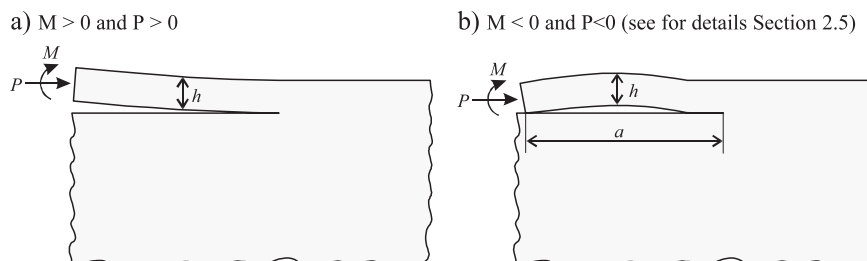


Fig. 4. Spalling of surface layer due to edge loads.

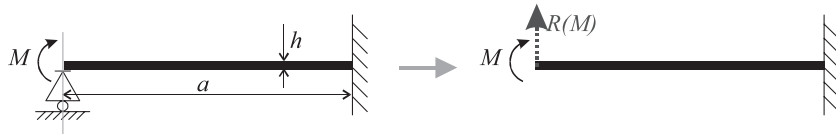


Fig. 5. Simple beam model for the determination of contact reaction in Fig. 4b. Reaction R is non-zero only in the case $M < 0$.

2.4. Crack tip contact

It is easily seen from the analytical solution (5) that K_I would become negative for some loading conditions, which means contact of the crack faces in the tip region. The normal stress on the contact area keeps K_I at zero. The FE results show that the contact extends over a distance of about $3h$ from the tip (Fig. 9). From the fact that the FE results in Fig. 8 do not much differ from the analytical curve, it can be concluded that the crack tip contact does not much affect the energy release rate G . So it appears that the analytical solutions (5)–(7) cover the cases of both edge and tip contact.

2.5. Contact conditions

Crack face contact occurs at the crack tip if Eq. (1) or Eq. (5) yields $K_I < 0$, and at the free edge of the debonded layer if it is curved downward, which is realized essentially in cases $M < 0$. Let us consider the second condition in more detail. The beam theory predicts (see Section 2.2, Eq. (4)) that the contact reaction $R \neq 0$ and correspondingly edge contact takes place in the case $M < 0$. The two-dimensional analysis (Ref. [14], Fig. A2) (based on Muskhelishvili method) points out some influence of P on vertical displacement and hence on the edge contact condition. The beam theory prediction for edge contact in form $M < 0$ follows from results of two-dimensional analysis under the restriction $P \ll -Ma/h^2$. For simplicity, we consider henceforth only

cases with $P \ll -Ma/h^2$ so that the contact condition becomes $M < 0$. So there are four possible combinations of contact and no contact (Table 1).

These cases have been grouped in to the two zones ($M > 0$ and $M < 0$, respectively) in loading parameter M – P plane with same rule for G computation within every zone. They can be graphically represented in the M – P plane as seen in Fig. 10. The condition $K_I = 0$ makes two straight lines (AC and AE) separating the parameter areas where crack tip contact is absent or present, according to Eqs. (1) and (5). The results in Fig. 8 justify the statement that for long cracks, the effect of crack tip contact on G is small or vanishing.

3. Convergent debonding

Debonding of layers attached to substrates typically involves three stages: initiation, steady-state propagation and a final transient as the debond converges on another debond. In the latter stage, the debonding crack can meet a neighbouring one, resulting in a layer chip spalling off. In the same way as in Ref. [11], we consider two debonding crack tips so close that their distance (ΔL in Fig. 11) is the only relevant length of the problem. The present approach extends the analysis in Ref. [11] by taking into account crack flank contact. The contact turns out to affect the G vs. ΔL relation considerably, as seen later in Fig. 15.

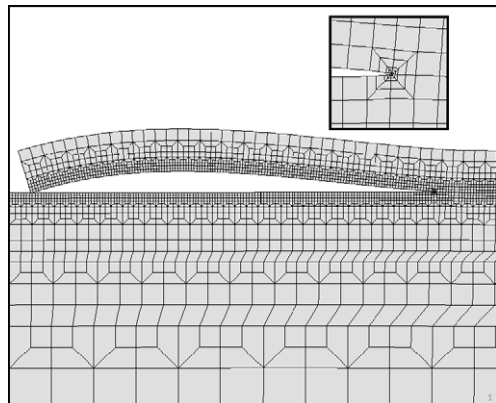


Fig. 6. Results of FE analysis for debonding of a surface layer with parameters $M = -0.00095Eh^2$, $P = 0.0029Eh$ corresponding to realistic TBC loading conditions $\epsilon_S = 0.6\%$, $\delta/h = 1$, $\epsilon_T = 1.5\%$. For details, see Section 4 and Appendix A. Displacements 10 times magnified.

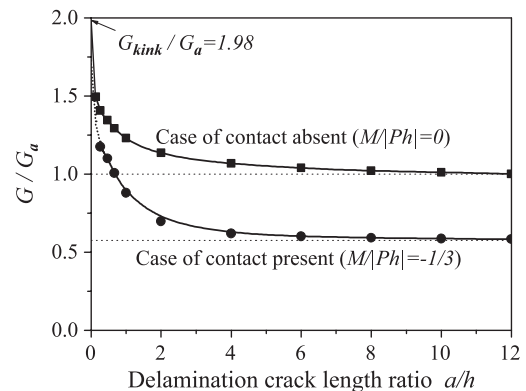


Fig. 7. Normalized energy release rate for a delamination crack; upper curve: after shrinkage due to sintering and subsequent cooling down; lower curve: after shrinkage due to sintering and renewed heating (loads as in Fig. 6); curves converging to the analytic solutions for $a/h \rightarrow \infty$ as well as for the kink edge $a/h \rightarrow 0$ with 1.98 for $M = 0$ and 1.74 for $M/|Ph| = -1/3$.

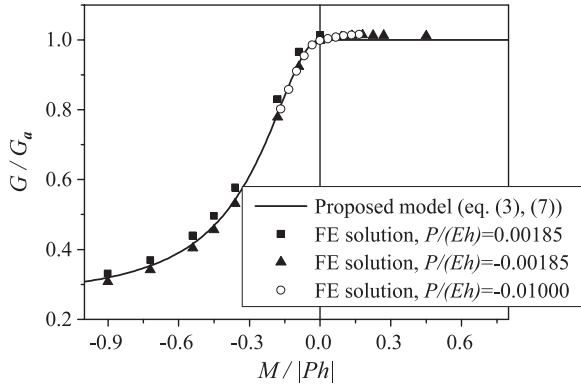


Fig. 8. Comparison of normalized energy release rate between analytical and FE results ($a/h \approx 10$) for various loading parameters P and M .

This effect of contact can be understood by the contact forces R acting at a distance l from the midplane as indicated in Fig. 11. Note that this is similar to the case of normal load in Ref. [12]. Stress intensity factors of the problem depicted in Fig. 11 are given by [18]:

$$K_I = \frac{R}{\sqrt{\pi\Delta L/2}} \left(\sqrt{\frac{2l + \Delta L}{2l - \Delta L}} + \sqrt{\frac{2l - \Delta L}{2l + \Delta L}} \right), K_{II} = 0. \quad (8)$$

With $G = \frac{1-\nu^2}{E} (K_I + K_{II})^2$ for plane strain conditions, this leads to

$$G = \frac{1-\nu^2}{E} \frac{8R^2}{\pi [1 - (\Delta L/2l)^2]} \frac{1}{\Delta L}. \quad (9)$$

So it appears that in the presence of contact, $G \sim 1/\Delta L$ in the limit of small ΔL (opposite to the case of no contact with $G \sim \Delta L$ by Ref. [11]), which means that spalling is inevitable once the debonding process has got into the final stage. This

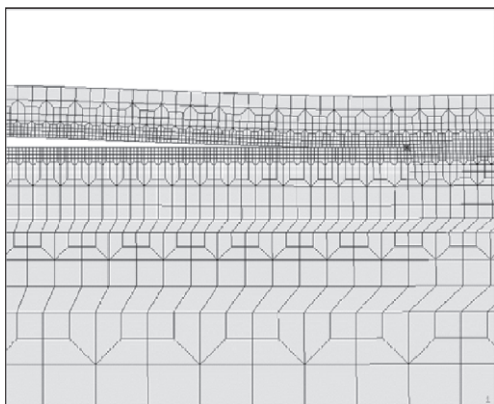


Fig. 9. Crack tip contact ($M = -0.000805Eh^2$, $P = -0.00657Eh$). Displacements 5 times magnified.

Table 1
Possible cases of crack face contact (tip contact assumedly does not influence G)

Case	Contact at crack tip, $K_I < 0$	Contact at edge, $M < 0$	Zone in Fig. 10	G
1	–	–	I	$\frac{1-\nu^2}{2Eh} \left(P^2 + 12 \frac{M^2}{h^2} \right)$
2	+	–	II	$\frac{1-\nu^2}{2Eh} \left(P^2 + 3 \frac{M^2}{h^2} \right)$
3	+	+		
4	–	+		

is in accordance with FE results in Fig. 15 for TBC configurations in Fig. 14b,c as can be seen later.

4. Application to laser-induced TBC debonding

4.1. Model for the analysis of TBC debonding

A simple two-dimensional model implying plane strain is applied for the analysis of debonding of TBC under thermal shock (Fig. 12a, compare with Fig. 1b). Because of the symmetry of the configuration, the representative element (Fig. 12b) contains only one crack.

The cyclic surface heating in the thermal fatigue test of TBC by means of laser irradiation leads to the progressive shrinkage due to sintering accompanying by high-temperature creep and simultaneous thermal expansion. This influence has been modeled by a stress-free strain tensor $\varepsilon_{ij}^{sf}(y) = \varepsilon_{ij}^S(y) + \varepsilon_{ij}^T(y)$. The stress-free strain due to sintering and creep is denoted here by ε_{ij}^S and leads to high tensile stress building up while cooling down to room temperature after cyclic heating. The stress-free strain due to temperature is denoted by ε_{ij}^T . For simplicity, ε_{ij}^S is supposed to be isotropic and homogeneous but confined to a certain depth δ

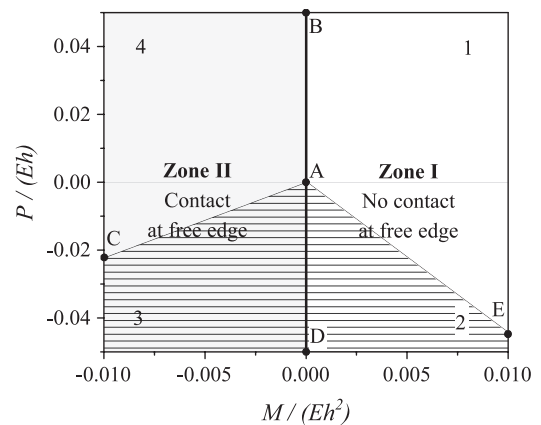


Fig. 10. Map of crack face contact in the M – P plane. Horizontal hatch means crack tip contact.

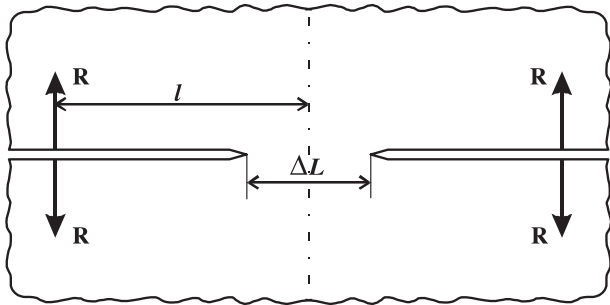


Fig. 11. Idealized debonding problem.

as indicated in Fig. 12c. This can be written with the Kronecker symbol δ_{ij} as $\varepsilon_{ij}^S = \begin{cases} -\delta_{ij}\varepsilon_S, & y = h - \delta \\ 0, & y < h - \delta \end{cases}$. The parameters ε_S and δ are understood to depend on the number of cycles, N . Strain ε_{ij}^T is approximated by a linear dependence across the layer (see Fig. 12c): $\varepsilon_{ij}^T = \delta_{ij}\varepsilon_T \frac{y}{h}$ with $\varepsilon_T = \alpha\Delta T$, where α is the linear thermal expansion coefficient and ΔT is the temperature difference across the layer. This approximation corresponds to an experimental situation where the characteristic heat diffusion depth at the end of the heating pulse is about equal to layer thickness h , which is approximately realized with 1-s heating time (see Fig. 3) as considered here. Residual stresses due to manufacturing are neglected in these considerations.

4.2. Finite element analysis of TBC delamination

Shrinkage in thermal cycling causes tensile stress leading to the initiation of vertical cracks whose spacing is comparable with TBC-layer thickness h (see Figs. 1a and 12a). As thermal cycling continues, the vertical cracks eventually turn into delamination cracks, which can be understood as follows. The energy release rate G of the vertical crack with infinitesimal kink along the interface increases as a result of progressive shrinkage as quantified here by the parameters ε_S and δ , which are increasing with N . As soon as G exceeds the interface toughness G_C , unstable debonding sets in which stops again at the position where $G=G_C$ (see Fig. 13), or slightly beyond as a result of dynamic effects. As the thermal cycling proceeds, further

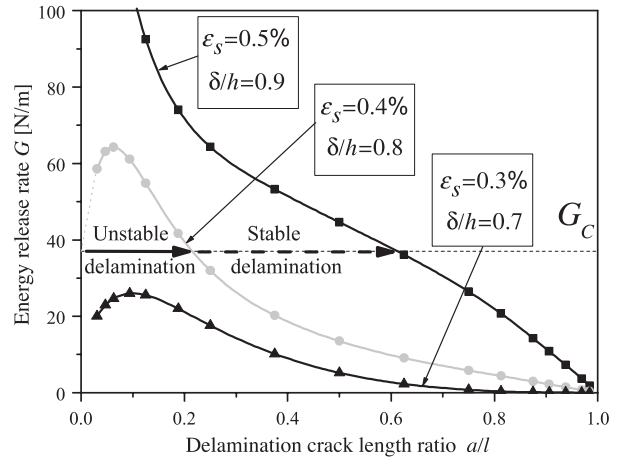


Fig. 13. Stable and unstable delamination with increasing ε_S and δ due to progressive sintering ($l=h$, $\varepsilon_T=0$).

propagation should be stable under the condition $G=G_C$ (see dashed arrow in Fig. 13).

The FE analysis has been done for a unit cell of TBC (see Fig. 12b) containing only one crack (fragment of FE mesh is given in Fig. 14a). The depth of the substrate H is taken as $10h$. The distance parameter l has been varied between $0.5h$ and $2h$; the numerical results are presented for $l=h$. The configuration is assumed to be loaded by shrinkage strains due to sintering and creep only, thermal strains being neglected here. The computations were performed with the following elastic moduli $E_1=85$ GPa, $E_2=215$ GPa, $\nu_1=0.18$, $\nu_2=0.3$ [19]. The interface toughness, $G_C=37$ N/m, has been taken from a four-point bending test modified by a stiffening layer [3,4]. The effect of mode mixity on G_C is neglected here (this effect has been considered in Ref. [3]). The computation of G has been performed for various crack lengths as indicated in Fig. 13.

4.3. Finite element analysis of contact driven TBC spalling

TBC spalling under thermal shock has been analysed with the same mesh as used in the analysis of delamination in Section 4.2. The possible configurations under the combined influence of sintering, creep and transient heating are seen in Fig. 14.

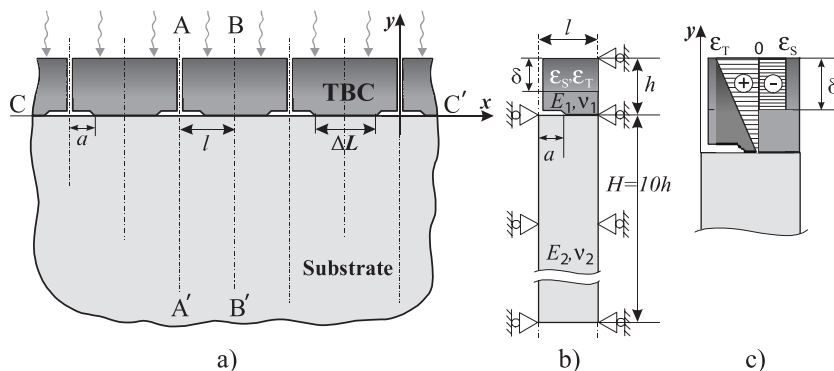


Fig. 12. Model for the analysis of TBC debonding.

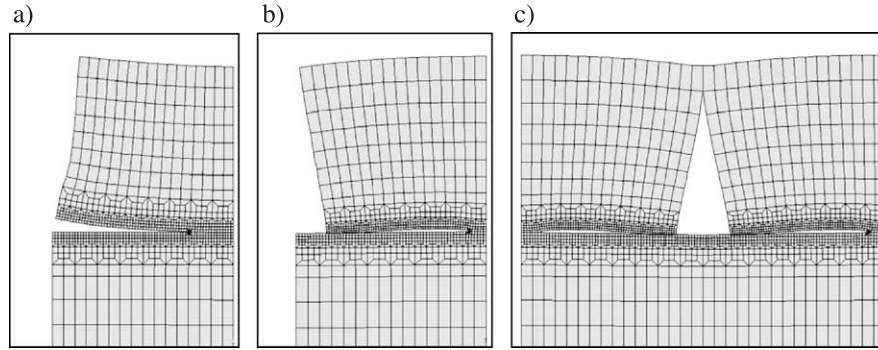


Fig. 14. Delamination cracks propagation in TBC: (a) without contact under sintering ($\varepsilon_s=0.4\%$, $\delta/h=0.8$, $\varepsilon_T=0$); (b) crack flank contact at horizontal parts under combined action of sintering and heating ($\varepsilon_s=0.6\%$, $\delta/h=1$, $\varepsilon_T=0.6\%$); (c) crack flank contact at both vertical and horizontal parts ($\varepsilon_s=0.6\%$, $\delta/h=1$, $\varepsilon_T=0.8\%$). Displacements 25 times magnified.

The debonding process is of a complex nature. There is an initial stage where shrinkage strain due to sintering is the main cause of stress. At this stage, maximum G is reached in the cooling phase of the thermal cycle, and the related analysis of TBC failure can be done by taking into account the sintering strain only, neglecting thermal strain. With the progress of crack propagation, a stage is reached where the effect of thermal strain is prevailing, leading to maximum G as a result of crack flank contact in the heating phase of the cycle.

The results of FE modelling are shown in Fig. 15 for the effect of sintering (Fig. 14a) and the combined effect of sintering and transient heating (see Fig. 14b,c). (Note that crack propagation means moving to the left in Fig. 15.) As the crack tips converge, the sintering-only curve becomes zero as it should, and agrees well with Eq. (9) in Ref. [11]. It is seen from Fig. 15 that with the effect of sintering only, crack propagation would stop at about $\Delta L/l \approx 0.2$, which means $a/l \approx 0.9$, so that there would be no complete detachment. Obviously, G is dramatically affected by the contact of the interface crack flanks: there is a mathematical divergence of G for $\Delta L/l \rightarrow 0$ (compare Eq. (9)), which is the cause of final detachment of the TBC layer fragments during the heating stage of the thermal cycle. It is also seen in Fig. 15 that partial contact at the vertical crack flanks eventually arising during the heating cycle makes a comparatively

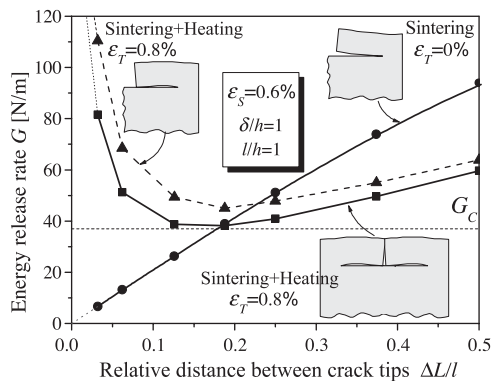


Fig. 15. Crack face contact due to inhomogeneous temperature leads to the progressive increasing of G with crack tips converge ($\Delta L/l \rightarrow 0$).

small contribution to the result. However, full contact at the vertical flank, which might arise in the high-temperature stage of the cycle, would remove the divergence of G .

The parameter regions of crack face contact combined with the presence or absence of the divergence of G are considered in Appendix A.

5. Conclusions

The multi-stage character of TBC-failure in thermal cycling, comprising vertical crack formation, delamination and spalling, has been analysed by taking into account crack flank contact in the transient high-temperature phase of the cycle. It has been shown that this crack flank contact can increase the energy release rate such that it can be responsible for final detachment or spalling. Without this newly proposed mechanism, the partly debonded layer fragments should be expected to remain attached to the substrate with some small area of their interface.

The wide-range analysis of contact driven delamination has been carried out both for small and for large cracks. The effect has been modelled by both a simple analytical approach and FE computations. The agreement of the results indicates that the modelling has been adequate to the problem.

Acknowledgement

The authors thank the Deutsche Forschungsgemeinschaft (DFG) for support within the priority program “Gradientenwerkstoffe” and the contract no. BA1411/5.

Appendix A. Crack face contact conditions for TBCs

This appendix is meant to apply the proposed models (5)–(7) and resulting contact conditions (Fig. 10) to the failure analysis for TBCs.

Cyclic surface heating of TBCs leads to sintering, creep, and thermal expansion whose combined effect is supposed to be adequately described by a function $\varepsilon_{xx}^{sf}(y)$, which is the horizontal component of stress-free strain tensor at vertical position y . This function is supposed to be known input data. According to the superposition principle of fracture mechanics, the stress field related to $\varepsilon_{xx}^{sf}(y)$ provides the same stress intensity factors as a force (see Fig. 4), $P = -\frac{E}{1-\nu} \int_0^h \varepsilon_{xx}^{sf}(y) dy$, and a moment about TBC mid-plane, $M = \frac{E}{1-\nu} \int_0^h \varepsilon_{xx}^{sf}(y) (y - \frac{h}{2}) dy$. With the special $\varepsilon_{ij}^{sf}(y)$ as considered in Section 4.1, we obtain

$$P = \frac{Eh\varepsilon_S}{2(1-\nu)} \left(2\frac{\delta}{h} - \frac{\varepsilon_T}{\varepsilon_S} \right), \tag{10}$$

$$M = \frac{Eh^2\varepsilon_S}{12(1-\nu)} \left[6\frac{\delta}{h} \left(1 - \frac{\delta}{h} \right) - \frac{\varepsilon_T}{\varepsilon_S} \right]. \tag{11}$$

So the steady-state energy release rate for absent crack flank contact at the edge (Eq. (3)) can be written as

$$G_a = \frac{1+\nu}{1-\nu} \frac{Eh\varepsilon_S^2}{8} \left\{ \left(2\frac{\delta}{h} - \frac{\varepsilon_T}{\varepsilon_S} \right)^2 + \frac{1}{3} \left[6\frac{\delta}{h} \left(1 - \frac{\delta}{h} \right) - \frac{\varepsilon_T}{\varepsilon_S} \right]^2 \right\}$$

(contact absent) (12)

and with Eq. (7) in the case of edge contact as

$$G_p = \frac{1+\nu}{1-\nu} \frac{Eh\varepsilon_S^2}{8} \left\{ \left(2\frac{\delta}{h} - \frac{\varepsilon_T}{\varepsilon_S} \right)^2 + \frac{1}{12} \left[6\frac{\delta}{h} \left(1 - \frac{\delta}{h} \right) - \frac{\varepsilon_T}{\varepsilon_S} \right]^2 \right\}$$

(contact present). (13)

With the simplifications mentioned in Section 2.5, $M=0$ in Eq. (11) makes a borderline between the horizontal contact and no-contact cases in a map of loading parameters, as in Fig. 10. As suggested by Eqs. (10) and (11), the map in Fig. 10 may be transformed by choosing δ/h and $\varepsilon_T/\varepsilon_S$ for loading parameters instead of P and M . In Fig. 16a, $M=0$ is represented by the parabola ODAB. There are more relevant

borderlines between zones in the parameter plane of Fig. 16a: The condition $K_I=0$ in Eqs. (1) and (5), combined with Eqs. (10) and (11), provides two lines, OEA and AC, separating the cases of present or absent crack tip contact. (The case of contact at the vertical crack flank as in Fig. 14c is discussed below in connection with Fig. 16b.) In the parameter area above the line OEAC, where the crack tip is closed, the validity of Eq. (12) must not be taken for granted, however, as the results in Fig. 8 suggest, is rather well realized.

Independent of the mapping derived from linear beam theory, we have got quite a number of FE results for configurations, which do not resemble a beam, as in Fig. 14. Sorting these results according to the presence or absence of crack face contacts has turned out rather well compatible with the zones in Fig. 16, which have been derived for beam-like configurations. Taking into account the eventually present contact at the vertical crack flank as in Fig. 14c makes an analogous map as seen in Fig. 16b. This map would depend on h/l , so we chose $h/l=1$ as in Fig. 14. (Points I, J, K in Fig. 16 correspond to configurations in Fig. 14a,b,c, respectively.) Absence or presence of contact at the vertical faces corresponds to the cases discussed in literature as “edge failure” and “inner failure”.

With the inequalities $M<0$ and $u_x>0$ along the line AA' in Fig. 12a, we obtained the conditions of divergence effect (Zone II in Fig. 16b) for $h/l=1$

$$6\frac{\delta}{h} \left(1 - \frac{\delta}{h} \right) < \frac{\varepsilon_T}{\varepsilon_S} < 6\frac{\delta}{h} \left(\frac{\delta}{h} - \frac{1}{3} \right). \tag{14}$$

The lower limit in Eq. (14) corresponds to crack face contact along the line CC' in Fig. 12a. It is represented by the line AB in Fig. 16. The upper limit in Eq. (14) corresponds to crack face contact along the line AA' in Fig. 12a. It is represented by the line AH in Fig. 16b. This line forms the boundary of Zone II where the divergence of G appears in convergent debonding. The zone III corresponds

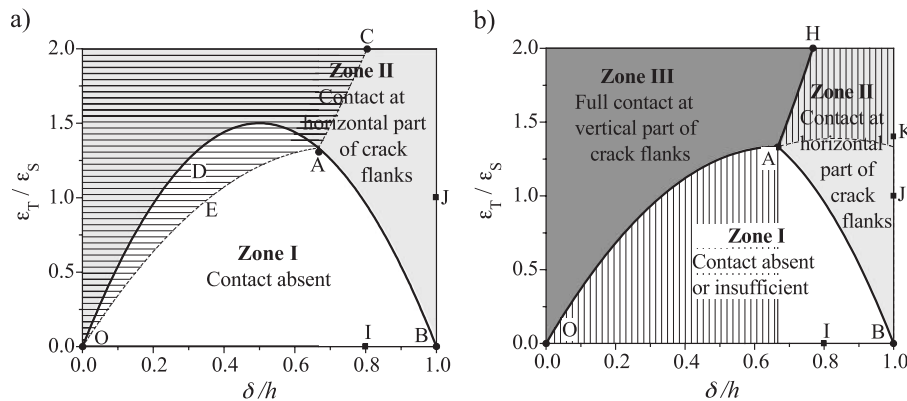


Fig. 16. Maps of crack face contact situations in the plane of loading parameters, zones derived from beam theory; (a) including contact at horizontal crack face only (as in Fig. 14b); (b) including contact at horizontal and vertical crack faces, for $h/l=1$ (as in Fig. 14c). Horizontal hatch means contact at crack tip. Vertical hatch means partial contact at vertical faces. Points I, J and K correspond to the situations presented in Fig. 14a, b and c accordingly.

to the full contact at vertical part of crack flanks. In this case, $G=0$ under steady-state conditions. The contact at crack tip in this case is absent.

As Fig. 16b involves analytical results for beam-like configurations which are supposed to be valid for $a \gg h$ in general and for $P \ll -Ma/h^2$ in the present contact problem, with neither condition being fulfilled in the cases considered here, it is surprising that the map has turned out compatible with the numerical results (for about 40 configurations) so that it can be stated that the present model has a rather wide field of applicability in connection with TBC debonding and spalling.

From a materials technology point of view, it is remarkable that the divergence of the G vs. crack length curve eventually leading to spalling failure of TBC may occur at an intermediate temperature in the thermal cycle, according to the present results. Additionally, it has also become obvious that the instant of maximum G vs. time during the cycle is shifting with increasing number of cycles. These results are expected to be valid for wide ranges of material parameters.

References

- [1] R.L. Loh, C. Rossington, A.G. Evans, J. Am. Ceram. Soc. 69 (1986) 139.
- [2] C.Y. Jian, T. Hashida, H. Takahashi, M. Saito, Compos. Eng. 5 (1995) 879.
- [3] H. Balke, H.-A. Bahr, A.S. Semenov, I. Hofinger, C. Häusler, G. Kirchhoff, H.-J. Weiss, in: K. Trumble, et al., (Eds.), Proceedings of 6th Int. Symposium on Functionally Graded Materials, Colorado, USA, September 10–14, 2000, Ceramic Transactions, vol. 114, 2001, p. 205.
- [4] H.-A. Bahr, H. Balke, T. Fett, I. Hofinger, G. Kirchhoff, D. Munz, A. Neubrand, A.S. Semenov, H.-J. Weiss, Y.Y. Yang, Mater. Sci. Eng. A362 (2003) 2.
- [5] P.R. Tavernier, D.R. Clarke, J. Appl. Phys. 89 (2001) 1527.
- [6] V. Tvergaard, Am. Ceram. Soc. 76 (1993) 729.
- [7] J.W. Hutchinson, Z. Suo, Adv. Appl. Mech. 29 (1991) 63.
- [8] W. Pompe, H.-A. Bahr, I. Pflugbeil, G. Kirchhoff, P. Langmeier, H.-J. Weiss, Mater. Sci. Eng. A233 (1997) 167.
- [9] H. Kirchhoff, Th. Göbel, H.-A. Bahr, H. Balke, K. Wetzig, K. Bartsch, Surf. Coat. Technol. 179 (2004) 39.
- [10] K. Klotz, H.-A. Bahr, H. Balke, Th. Göbel, S. Menzel, U. Bahr, G. Kirchhoff, K. Wetzig, Thin Solid Films 413 (2002) 131.
- [11] M.Y. He, A.G. Evans, J.W. Hutchinson, Acta Mater. 45 (1997) 3481.
- [12] A.G. Evans, J.W. Hutchinson, M.Y. He, Acta Mater. 47 (1999) 1513.
- [13] J.W. Hutchinson, A.G. Evans, Surf. Coat. Technol. 149 (2002) 179.
- [14] M.D. Thouless, A.G. Evans, M.F. Ashby, J.W. Hutchinson, Acta Metall. 35 (1987) 1333.
- [15] M. Comninou, J. Appl. Mech. 44 (1977) 631.
- [16] R. Rice, J. Appl. Mech. 55 (1988) 98.
- [17] MSC.Marc, Volume A: Theory and User Information. MSC Software, Los Angeles, CA, 2000.
- [18] H. Tada, P.C. Paris, G.R. Irwin, The Stress Analysis of Cracks Handbook, Dell Research Corporation, Hellertown, 1973.
- [19] U. Leushake, PhD Thesis, RWTH Aachen, Germany, 2001.